energies

MDPI

Article

A Witricity-Based High-Power Device for Wireless Charging of Electric Vehicles

Zhongyu Dai, Junhua Wang *, Mengjiao Long and Hong Huang

School of Electrical Engineering, Wuhan University, Wuhan 430072, China; zhongyudai_gt@163.com (Z.D.); longmj960@gmail.com (M.L.); honghuang94@foxmail.com (H.H.)

* Correspondence: junhuawang@whu.edu.cn; Tel.: +86-27-6877-6608

Academic Editor: Sheldon S. Williamson

Received: 14 January 2017; Accepted: 1 March 2017; Published: 7 March 2017

Abstract: In this paper, a Witricity-based high-power device is proposed for wireless charging of electric vehicles. According to the specific requirements of three-stage charging for electric vehicles, four compensation modes of the Witricity system are analyzed by the Loosely Coupled Theory among transformer coils and the Substitution Theorem in circuit theory. In addition, when combining voltage withstand levels, the current withstand capability, the switching frequency of electronic switching tubes, and the features of the resonant circuit, the series-parallel (SP) compensation mode is selected as the best compensation mode for matching the capacitor of the system. The performances of coils with different ferrite core arrangements are compared by simulations and models. The feasibility of the system is verified theoretically and the system functions are evaluated by the joint simulation of Simplorer and Maxwell. Finally, a Witricity-based high-power device is proposed as designed, and the correctness of theoretical analyses and simulation results are verified.

Keywords: electric vehicles; Witricity; the joint simulation; compensation modes; high-power device

1. Introduction

Witricity technology has received much attention and realized rapid development since the concept was recalled in 2007 [1]. This technology based on magnetic resonance coupling can transfer the electric energy or power over a distance without the use of wires. It has been playing an important role in various fields from daily products to medical equipment and aerospace fields [2–8]. Especially in recent years, the number of electric vehicles has increased rapidly. However, more and more people have realized that there are essential limitations on the charger for the wide-spread applications of environmentally friendly electric vehicles. Therefore, researchers are paying more attention to research into wireless charging technology for electric vehicles [9–19].

There are two typical charging modes for electric vehicles, namely constant current and constant voltage mode. Under the consideration of battery characteristics and charging speed performances, the three-stage charging method is the most commonly used method in practice, wherein the charging process starts with a constant current and a rapidly increased voltage. When the voltage reaches a specified level, the charger goes into the constant voltage mode until the charging current decreases to nearly zero. Therefore, the charging system can not only be equivalent to a constant current source but also to a constant voltage source when Witricity technology is used to charge electric vehicles.

In this paper, four compensation modes were analyzed based on the theory of the loosely coupled transformer and the equivalent circuit model, namely Model A and Model B. Only the series-parallel (SP) compensation mode and the parallel-series (PS) compensation mode can meet the requirements for the system can be equivalent to a constant current or a constant voltage source. Considering the characters of the electronic components and the performance of the power source, such as the withstand voltage, the withstand current, the switching frequency, and the ripple voltage, the SP

compensation mode is suitable for the system. The simulations based on the joint simulation of Simplorer and Maxwell also have been conducted for coils with different ferrite cores to select the best match. Finally, a Witricity-based high-power device was proposed. The experiments also have been carried out to test the theory and the simulation results, and explanations for the discrepancy between the experimental results and the theoretical results are demonstrated.

2. Fundamental Analysis

Series resonant and parallel resonant are the two basic resonant modes. In the Witricity circuit, the primary and secondary sides both need to be compensated with a resonant capacitor. Figure 1 shows the four compensation modes; series-series (SS) compensation, series-parallel (SP) compensation, parallel-series (PS) compensation, and parallel-parallel (PP) compensation.

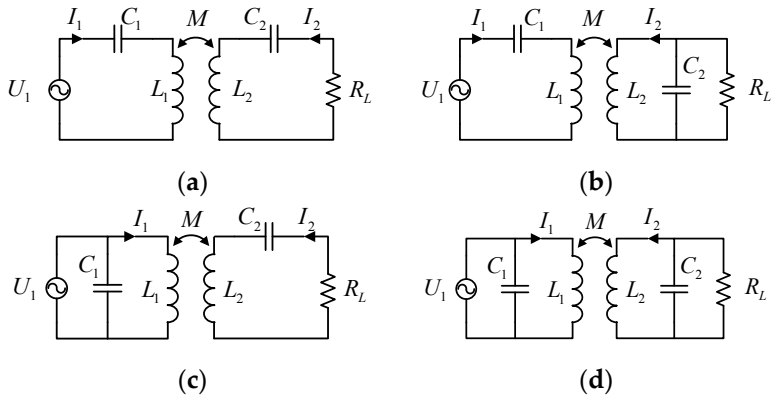

Figure 1. Four compensation modes. (**a**) series-series (SS) compensation; (**b**) series-parallel (SP) compensation; (**c**) parallel-series (PS) compensation; (**d**) parallel-parallel (PP) compensation.

In the Witricity system, the inductance of the coil and the compensation capacitance should be matched to constitute a resonance circuit with a fixed operation frequency. The values of C_1 and C_2 are chosen such that:

$$\begin{aligned} f_r &= \frac{1}{2\pi\sqrt{L_1C_1}} \\ f_r &= \frac{1}{2\pi\sqrt{L_2C_2}} \end{aligned} \tag{1}$$

For simplicity, the circuit should be equivalently transformed to analyze the characteristics. Figure 2 shows the equivalent transformation process of the circuit, where Z_{11} and Z_{22} are the primary and secondary total impedances, respectively. The equivalent circuit A, based on the loosely coupled transformer, is shown in Figure 2a. In Figure 2b, the circuit based on the nature of ideal transformer is decoupled, namely the equivalent circuit B.

$$\begin{aligned} Z_{eq} &= \frac{(\omega M)^2}{Z_{11}} or Z_{eq} = \frac{(\omega M)^2}{Z_{22}} \\ u_0 &= \frac{j\omega M u_1}{Z_{11}} \end{aligned} \tag{2}$$

In the following, the equivalent circuits A and B are used to analyze the equivalent transformation of the four compensation modes in the Witricity circuit.

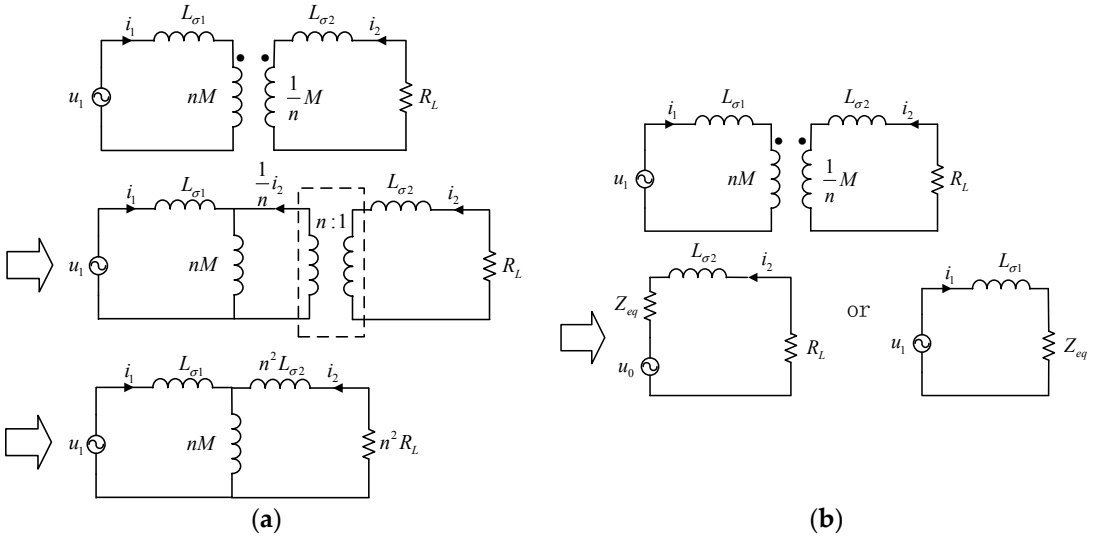

Figure 2. The equivalent circuit. (**a**) The equivalent circuit A; (**b**) The equivalent circuit B.

2.1. The SS Compensation Circuit

Figure 3 shows the equivalent transformation process of the SS compensation Witricity circuit based on the equivalent circuit A, where C_1 and $\frac{C_2}{n^2}$ are chosen to resonate with L_1 and n^2L_2 in Equation (1). Thus, the Witricity circuit can be equal to a load-independent voltage source.

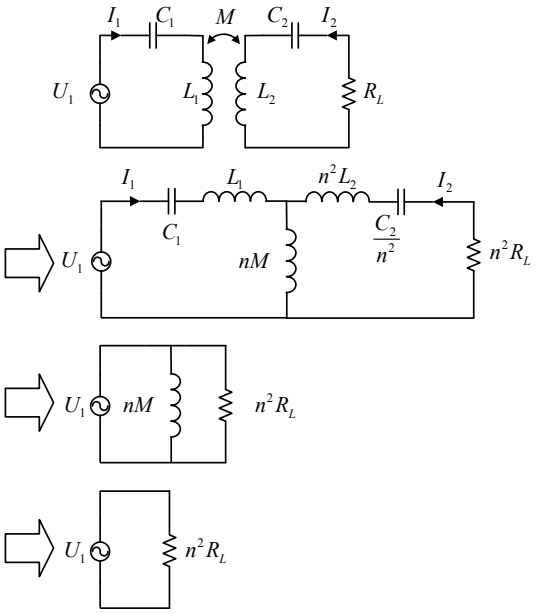

Figure 3. The SS compensation Witricity circuit using the equivalent circuit A.

When using the equivalent circuit B to equivalently transform the SS compensation Witricity circuit, the secondary equivalent impedance Z_{eq} is calculated as:

$$Z_{eq} = \frac{(\omega M)^2}{j\omega L_1 + \frac{1}{j\omega C_1} + R_L} = \frac{(\omega M)^2}{R_L} \tag{3}$$

The equivalent change process is shown in Figure 4.

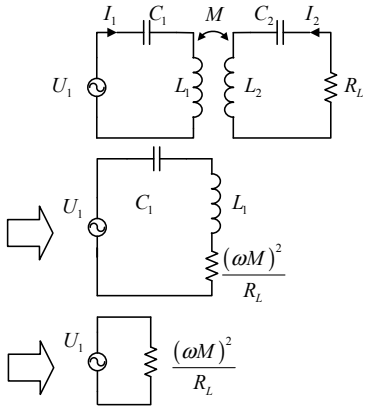

Figure 4. The SS compensation Witricity circuit using the equivalent circuit B.

The SS compensation Witricity circuit can only be equivalent to an ideal voltage source from the above analysis.

2.2. The SP Compensation Circuit

Figure 5 shows the SP compensation Witricity circuit equivalent change process using the equivalent circuit A. Obviously, the Witricity circuit can be equal to an ideal current source.

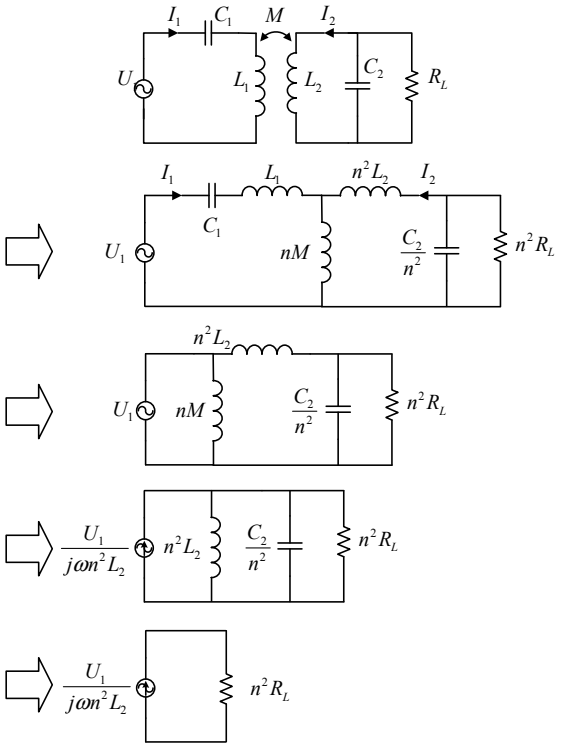

Figure 5. The SP compensation Witricity circuit using the equivalent circuit A.

If the SP compensation Witricity circuit equivalently transforms according to the equivalent circuit A, the secondary equivalent impedance Z_{eq} would be given by:

$$Z_{eq} = \frac{(\omega M)^2}{j\omega L_2 + \frac{\frac{1}{j\omega C_2} \times R_L}{\frac{1}{j\omega C_2} + R_L}} = \frac{(\omega M)^2}{j\omega L_2 + \frac{R_L}{1 + j\omega C_2 R_L}} \tag{4}$$

From (1), it is known that $\omega L_2 = \frac{1}{\omega C_2}$. Therefore, (4) can be simplified into:

$$Z_{eq} = \frac{M^2 R_L}{{L_2}^2} - j\omega \frac{M^2}{L_2} \tag{5}$$

If a series inductance $L_S = \frac{M^2}{L_2}$ is added to the primary circuit, the Witricity circuit can be equivalent to a load-independent voltage source, shown in Figure 6.

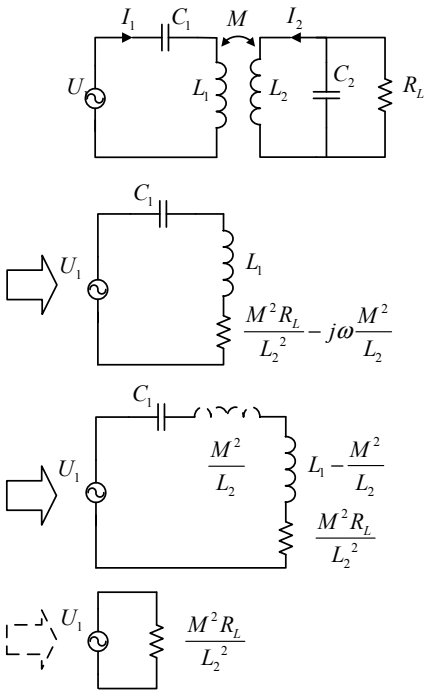

Figure 6. The SS compensation Witricity circuit using the equivalent circuit B.

From the above analysis of the SP compensation Witricity circuit by using the equivalent circuit A and B, the Witricity circuit can be equivalent to not only an ideal current source but to an ideal voltage source as well.

2.3. The PS and PP Compensation Circuit

Similar to the analysis presented in Sections 2.1 and 2.2, the PS and PP compensation circuit equivalent transformation process on the basis of equivalent circuit A is shown in Figure 7.

If a compensation capacitance C_S is added to the designed circuit to resonate with the inductance $\frac{nL_1M}{L_1+nM}$, the Witricity circuit is a load-independent voltage source. Similar to the PS compensation circuit, when a compensation capacitance C_S is added to meet the capacitance $C_S + \frac{C_2}{n^2}$ and resonates with the inductance $\frac{nL_1M}{L_1+nM} + n^2 L_2$, the Witricity circuit can be equal to a load-independent current source, and the current can be calculated by:

$$I_0 = \frac{MU_1}{j\omega(L_1M + nL_1L_2 + n^2ML_2)} \tag{6}$$

Figure 8 shows the equivalent change process of the PS and PP compensation Witricity circuit using the equivalent circuit B.

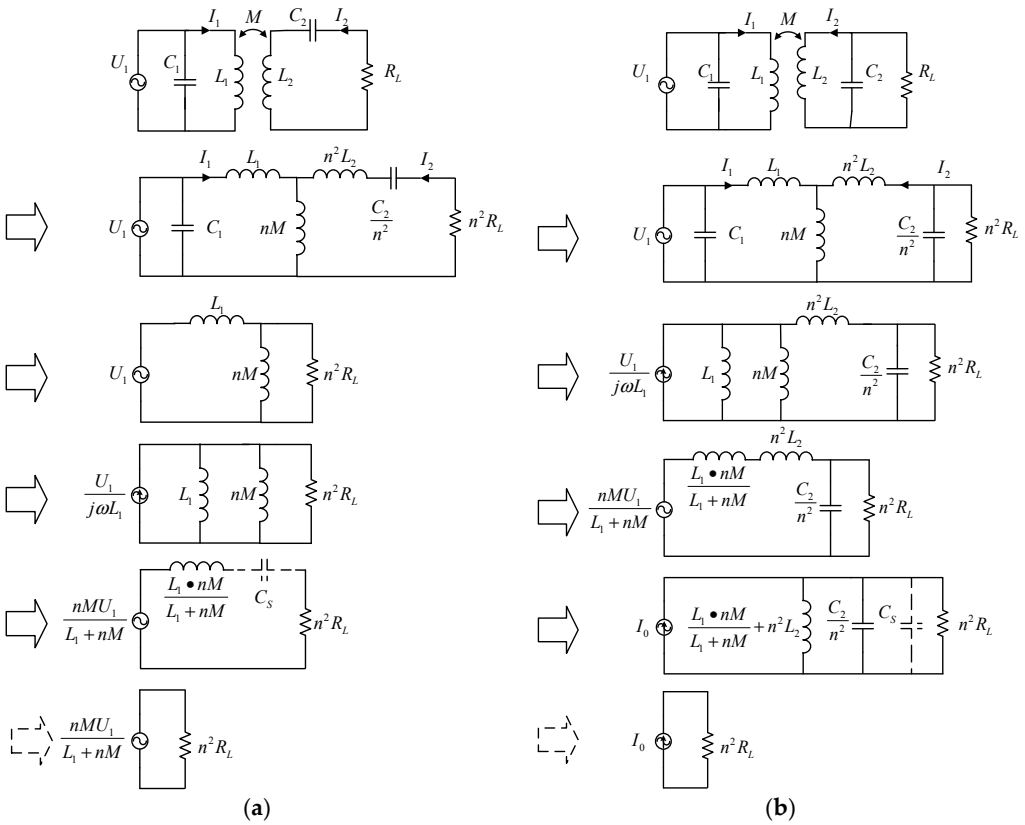

Figure 7. The SP and PP compensation Witricity circuit using the equivalent circuit A. (**a**) The SP compensation Witricity circuit; (**b**) The PP compensation Witricity circuit.

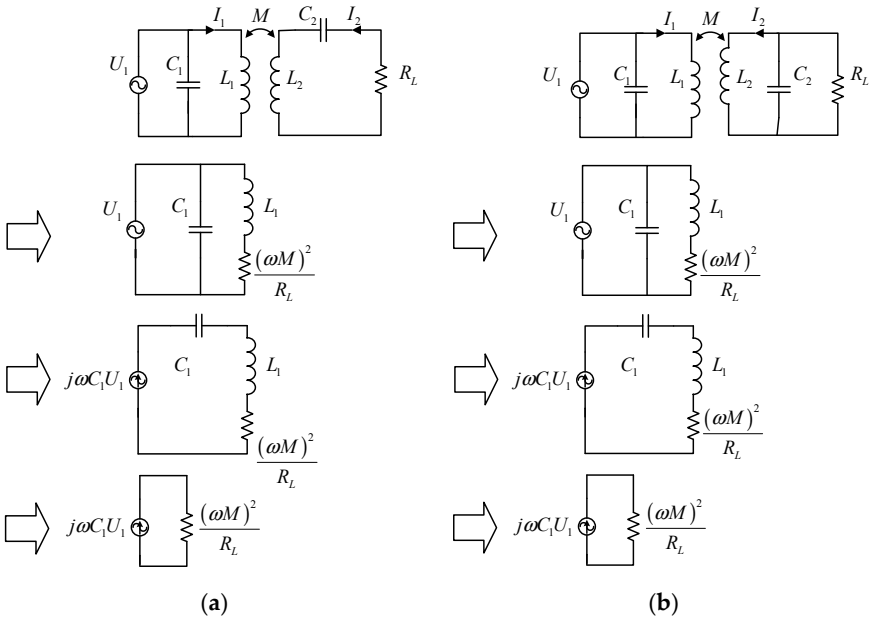

Figure 8. The SP and PP compensation Witricity circuit using the equivalent circuit B. (**a**) The SP compensation Witricity circuit; (**b**) The PP compensation Witricity circuit.

In Figure 8, the PS compensation Witricity circuit is a load-independent current source after equivalent change, while the PP compensation Witricity circuit is a load-independent voltage source.

From the above equivalent simplification of four kinds of compensation circuits, it is obvious that the SS and PP compensation Witricity circuit can only be equal to a load-independent current or voltage source, while the SP and PS compensation Witricity circuit is not only a load-independent current source but also a load-independent voltage source when a matched capacitance or inductance is added to the circuit. If Witricity technology is used to charge the electric vehicle, it should meet the requirement of the most commonly used charging scheme, also called three-stage charging, which contains two dominant charging stages of constant current and constant voltage modes. In other words, the circuit is required to be equivalent to a load-independent current source and a load-independent voltage source at the same time. Therefore, we can draw a conclusion from above analyses that only the SP and PS compensation Witricity circuit can meet the requirements.

In the resonant circuit, the quality factor Q can be calculated by:

$$Q = \frac{\omega L}{R} = \frac{1}{R}\sqrt{\frac{L}{C}} \tag{7}$$

In the inductance-capacitance (LC) series resonance circuit, it is well known that the voltage values on L and C are identical, while the phases are opposite. Thus the sum of the two voltage vectors is zero, and the withstand voltage of the input power source can be reduced. However, the voltages of the L and C are Q times the input voltage in the LC parallel resonance circuit. As a consequence, the withstand voltage of the input power source may be Q times its supply. In the meantime, much of the reactive current is delivered between the inductance L and the capacitance C in the LC parallel resonance circuit. Hence, the load can receive more active power. For the device based on Witricity technology, the electronic switching tube is the most important device, deciding the performance of the whole device. The electronic switching tube usually can withstand high current but not high voltage. Therefore, the LC series compensation mode is chosen in the primary circuit. For the secondary circuit, to output more active power, the LC parallel compensation mode is better. For other parts of the circuit structure, a three phase full-bridge controlled rectifier, a full bridge inverter, and a full-wave rectifier are chosen. Above all, the SP compensation Witricity circuit selected for high-power wireless charging of electric vehicles is shown in Figure 9.

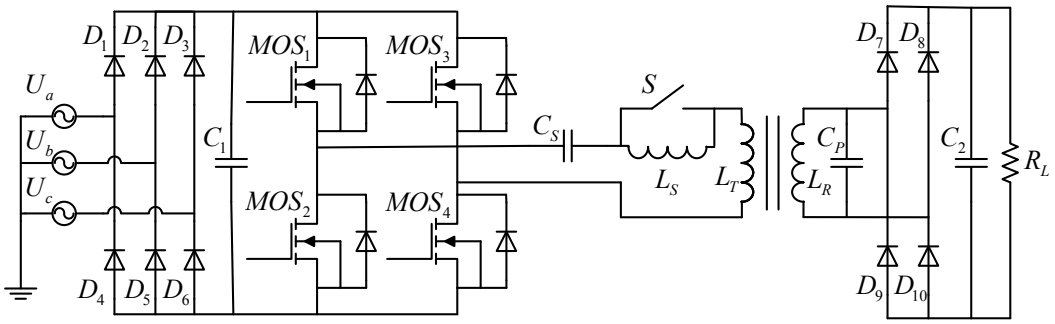

Figure 9. High-power wireless charging circuit of electric vehicles with SP compensation.

3. Simulation

The square coil and the circular coil are the typical structures used in the Witricity circuit. Figure 10 shows their magnetic field distributions based on simulation. Obviously, for the square coil, there are magnetic abnormalities because of its rectangular structure, which may decrease the sufficiency of power traction and utilization and increase the temperature. Especially when the transmission power is large, the disadvantages are much more obvious. Therefore, the circular coil is a better selection for the Witricity circuit.

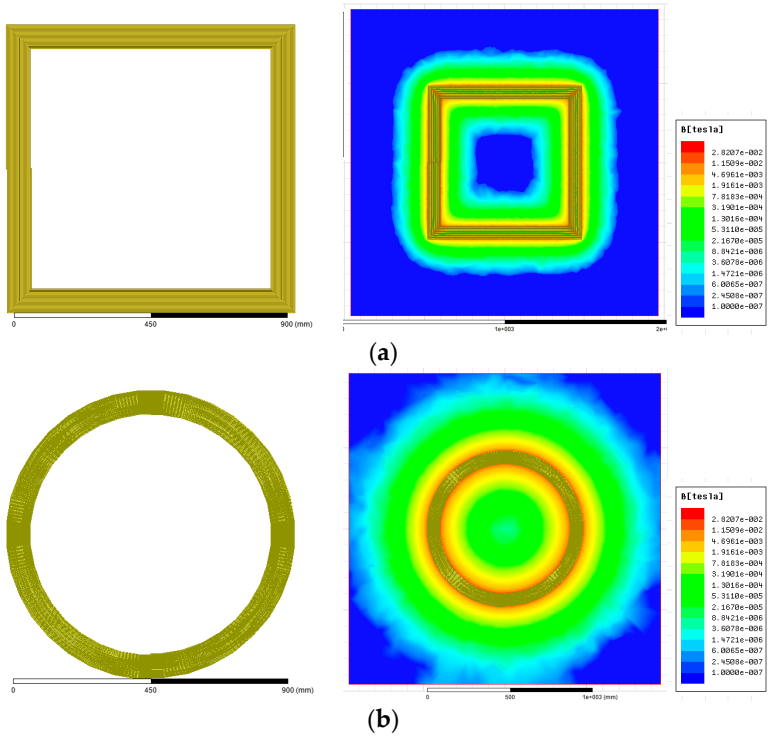

Figure 10. The magnetic flux distributions. (**a**) The square coil; (**b**) The circular coil.

To improve the coupling efficiency between the coils and reduce the leakage of the magnetic field, ferrite cores are added to the coils. Figure 11 shows some simulation of coils with different ferrite cores, which have been conducted to compare the performances in order to increase the coupling coefficient. The coupling coefficient representing the coupling degree between coils can calculated by:

$$\kappa = \frac{M}{\sqrt{L_1 L_2}} \tag{8}$$

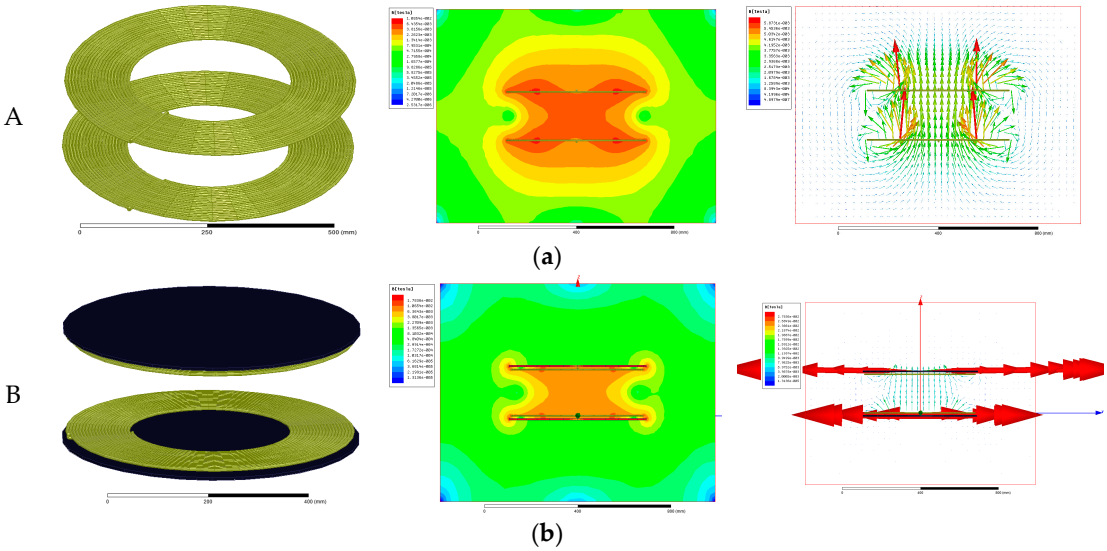

Figure 11. *Cont.*

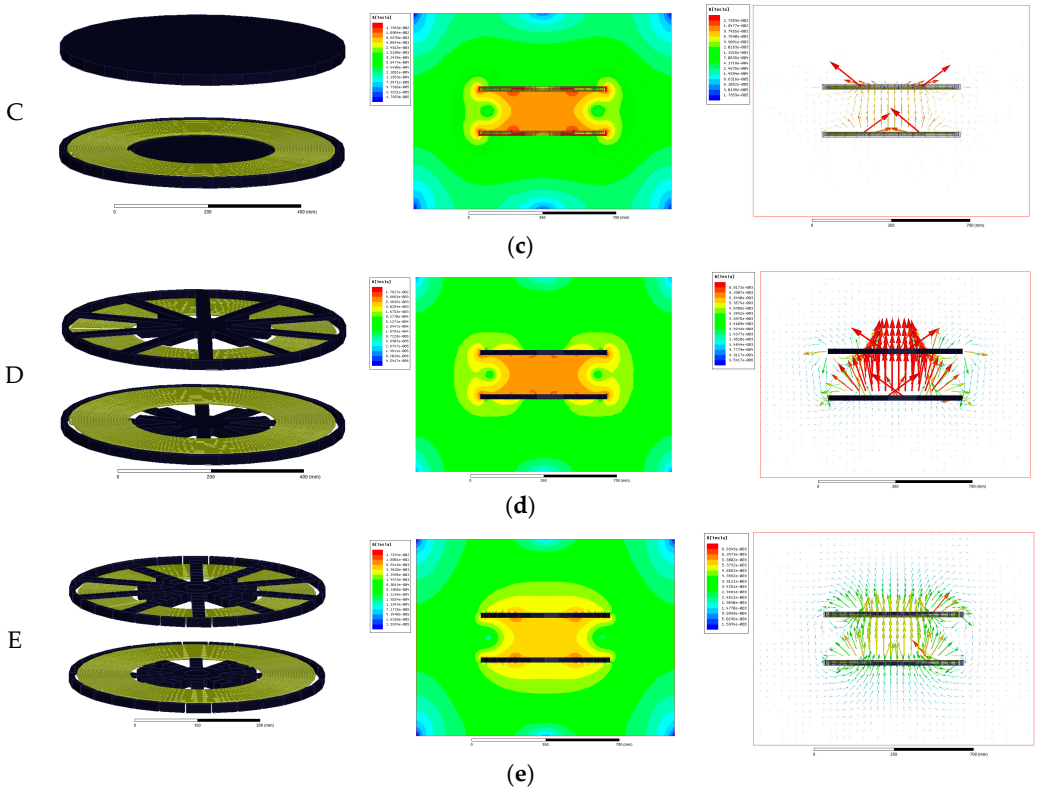

Figure 11. The coils with different ferrite cores, the magnetic flux distributions, and the magnetic line distributions. (**a**) A-without ferrite cores; (**b**) B-with a flat plate ferrite core; (**c**) C-with an "E" ferrite core; (**d**) D-with a hollow "E" ferrite core; and (**e**) E-with an improved hollow "E" ferrite core.

It is well known that the transmission efficiency is closely correlated with the direction of the magnetic lines. The magnetic flux distributions and the magnetic line distributions of the five coils with different ferrite cores have been shown in Figure 11. Obviously, for coil A without a ferrite core, most of the magnetic lines through the coil are used to transmit power, but there are some magnetic lines leaking through the air. Compared with coil A, the direction of the magnetic lines is constrained so that more of them pass through the coils to increase the transmission efficiency in coil B with a flat plate ferrite core. From Figure 11, the transmission efficiency of coil C with an 'E' ferrite core is the highest. Coil D with a hollow 'E' ferrite core has almost the same transmission efficiency as coil C, but the weight of the ferrite core is about half that of coil C. Coil E has an improved hollow 'E' ferrite core, made up of small ferrite core pieces, which are inexpensive and easy to obtain, but the binding effect of the magnetic lines drops rapidly.

Table 1 and Figure 12 reveal that the self-inductance, mutual-inductance, and coupling coefficient of coil C are the highest of all, and the coupling coefficient of coil D is slightly lower. However, the amount of ferrite core in coil D is just about half of that in coil C, which cuts the costs and reduces the weight. Thus coil D is a better choice for the Witricity circuit for wireless charging of electric vehicles.

Table 1. Self-inductance, mutual-inductance, and coupling coefficient of five different coils.

Name	Self-Inductance (μH)	Mutual-Inductance (μH)	Coupling Coefficient
A	229.63	42.692	0.186
B	357.37	91.931	0.257
C	421.32	121.08	0.287
D	398.38	111.92	0.281
E	259.98	53.978	0.208

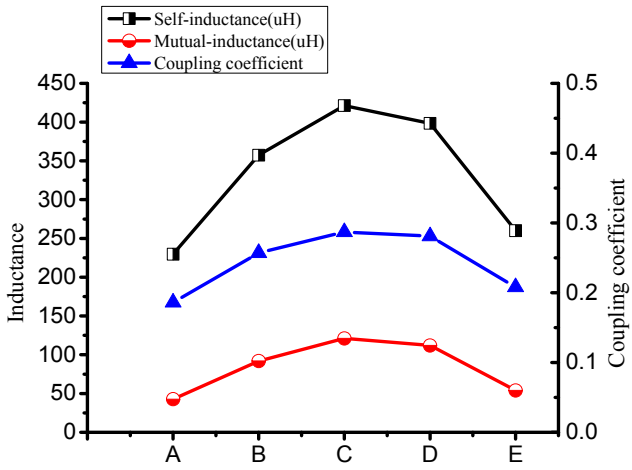

Figure 12. Self-inductance, mutual-inductance, and coupling coefficient of five different coils.

Through the discussion above, the simulation of the Witricity system based on the joint simulation method of Simplorer and Maxwell is carried out, as shown in Figure 13. The SP compensation Witricity circuit model is built according to Simplorer and the coil identified in Maxwell. In order to make the coils work under the fixed operating frequency, $f = 100$ kHz, the coils must be revised with the compensation capacitance $C_S = C_P = 6358$ pF.

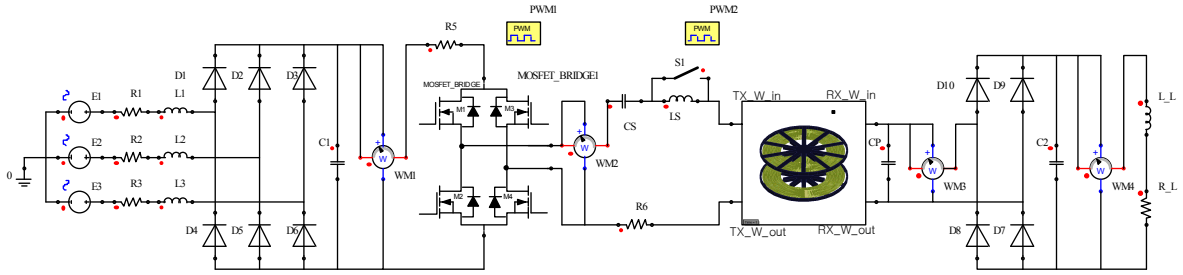

Figure 13. The joint simulation method of Simplorer and Maxwell.

The joint simulation results are shown in Figure 14. To simplify the analysis and recognize the results more clearly, Figure 14a,b show the results from 0 to 100 ms, while Figure 14c–f is from 40 to 40.1 ms. The three-phase input voltage is shown in Figure 14a. The amplitudes are 311 V, while the phase difference between them is 120°. The DC voltage is obtained after a three-phase uncontrolled rectifier, on a scale of 480 V to 536 V, as shown in Figure 14b. It is easy to find that, within the fluctuation frequency, $f_t = 300$ Hz, the value of the DC voltage is nearly unchanged within 0.1 millisecond. In Figure 14c, WM1.V is the DC voltage of about 536 V, WM2.V represents the square voltage obtained after full bridge inverter within the frequency, $f_C = 100$ kHz, and WM3.V is the secondary voltage, the waveform of which is similar to the sine wave within frequency $f_S = f_C = 100$ kHz. Figure 14d shows the current. WM2.I is the rectified current. WM2.I and WM3.I represent the primary current and secondary current, respectively, which are similar to the sine wave within the frequency $f_C = 100$ kHz, and their amplitudes are about 7.5 A and 8.2 A. In Figure 14e, WM1.P is the output power of the full-wave bridge rectifier, which has almost the same waveform as WM2.P, the primary power, the shape of which can be approximated as a sine function $p_1 = p_2 = 3.7 \times \left|\sin(2 \times 10^5 \pi t)\right|$. Similarly, the sine function $p_3 = 2.05 + 2.05 \times \sin(4 \times 10^5 \pi t + \pi/2)$ is fit for WM3.P, the secondary power. For Figure 14f, WM3.I, WM3.V, and WM3.P are the input current, the voltage, and the power of the secondary side, respectively, of the full-wave bridge rectifier, while WM4.I, WM4.V, and WM4.P are the output of the full-wave bridge rectifier. It can be concluded from Figure 14f that there is hardly

any power loss for the full-wave bridge rectifier. It is well known that the average efficiency is similar to the efficiency of energy transfer in a time period. W_1 and W_4 are the input energy and the output energy in a time period, respectively, and can be derived by:

$$\begin{array}{l} W_1 = \int_0^{T_1} p_1 dt \approx \int_0^{T_3} p_2 dt \\ W_4 = \int_0^{T_1} p_4 dt \approx \int_0^{T_3} p_3 dt \end{array} \quad (9)$$

Therefore, the overall efficiency of the Witricity circuit can be calculated by:

$$\eta = \frac{W_4}{W_1} \approx 87\% \quad (10)$$

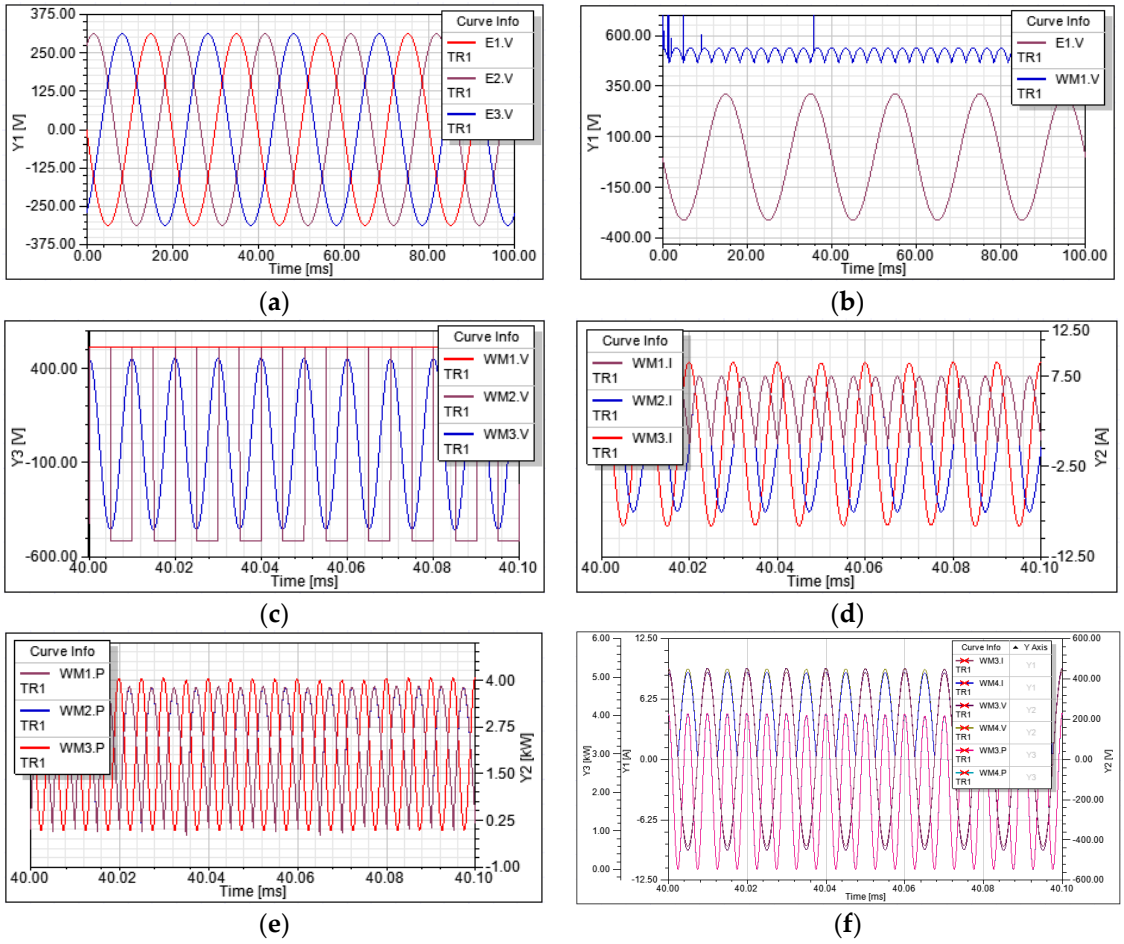

Figure 14. The joint simulation results. (**a**) The three-phase input voltage; (**b**) The three-phase uncontrolled rectifier; (**c**) The voltage of the rectifier terminal, primary side, and secondary side; (**d**) The current of the rectifier terminal, primary side, and secondary side; (**e**) The power of the rectifier terminal, primary side, and secondary side; (**f**) The full-wave bridge rectifier of the secondary side.

4. Experimental Evaluation

To verify the above analysis, a high-power device based on Witricity technology for the wireless charging of electric vehicles has been built with the SP compensation mode, as shown in Figure 15.

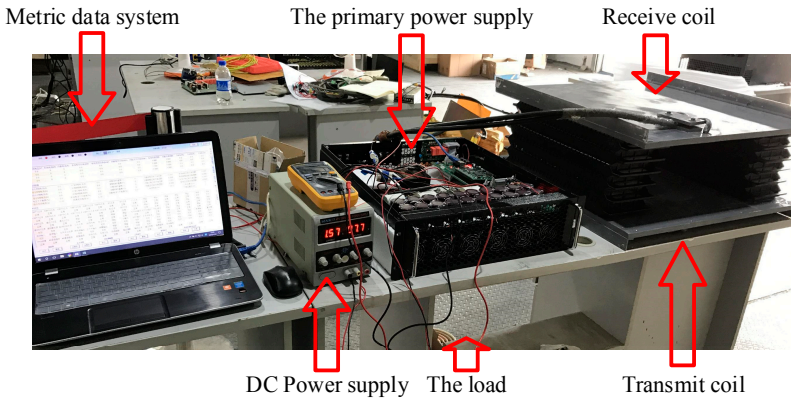

Figure 15. A Witricity-based high-power device for the wireless charging of electric vehicles.

In the experiment, the distance between the transmitting and the receiving coil is 30 cm, the input voltage has the commercial power of 380 V, and the compensation capacitance is 7 nF. Through adjusting the input power, the transformer parameters can be measured and are listed in Table 2.

Table 2. The measured parameters of the input side and the output side.

Input Voltage (V)	Input Current (A)	Input Power (kW)	Output Voltage (V)	Output Current (A)	Output Power (kW)	Transmission Efficiency
254	29.4	7.47	426	14.18	6.04	80.91%
275	32.9	9.08	475	15.59	7.40	81.55%
293	35.8	10.5	513	16.93	8.68	82.69%
315	38.5	12.19	565	17.77	10.03	82.31%
330	41.8	13.82	614	18.46	11.32	81.88%
346	44.7	15.5	649	19.18	12.44	80.24%
357	47.4	16.98	688	19.76	13.59	80.02%
364	49.5	18.03	714	20.59	14.70	81.55%
371	51.7	19.19	738	20.86	15.39	80.19%
378	52.8	19.95	751	21.34	16.02	80.32%

From Figures 16 and 17, the voltage, the current, and the power of the device's output side increase with the change of the input side. The changing rate of the input voltage is slower than the secondary side, while the changing rate of the current is the opposite of the voltage's changing tendency. This is because the secondary voltage has been designed on the standard interfaces and protocols of the DC charge spots, the output voltage of which ranges from 250 V to 750 V. However, the input voltage can only change from 0 to 380 V.

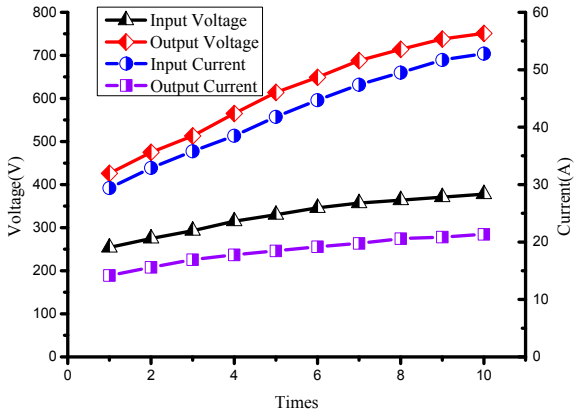

Figure 16. The input voltage, the output voltage, the input current, and the output current.

The trends of the input voltage, input current, output voltage, and output current are shown in Figure 16, while the power and the transmission efficiency are shown in Figure 17.

Figure 17 shows the measured transmission efficiency fluctuating around 0.81 with the change of the transmission power, which is lower than the theoretical result. Through analyses and summary, some reasons can be concluded as follows.

(a) The simulation model, built in an ideal circumstance, has less power loss than the actual circuit.
(b) The electromagnetic shielding effectiveness of the ferrite core, which is made of small blocks, is worse than the whole ferrite core built in Maxwell.
(c) There are measurement error and other extraneous factors affecting the transmission efficiency.

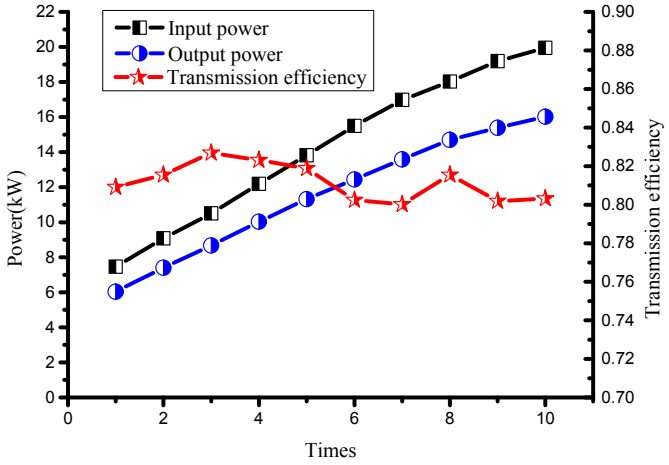

Figure 17. The power and the transmission efficiency.

5. Conclusions

Based on the Witricity concept and the compensation mode research, one application method for the wireless charging of electric vehicles is proposed and studied through simulations and experiments. In addition, four compensation modes have been analyzed to find the one best suited to the circuit. The joint simulation of the Witricity system based on Simplorer and Maxwell was carried out as well. The experimental results are presented to evaluate the performance of the derived prototype, and reasons for the differences between the measured parameters and the theoretical result have been concluded.

Acknowledgments: This work was supported in part by the National Natural Science Foundation of China (Grant Number 51507114) and in part by the Natural Science Foundation of Hubei Province (Grant Number 2014CFB272).

Author Contributions: Zhongyu Dai proposed the compensation mode and coil structure, conducted the modeling analysis, and performed the experiments. The manuscript was improved and revised by Junhua Wang, Mengjiao Long, and Hong Huang. All of the authors contributed to the paper writing.

Conflicts of Interest: The authors declare no conflict of interest.

References

1. Karalis, A.; Joannopoulos, J.D.; Soljačić, M. Efficient wireless non-radiative mid-range, energy transfer. *Ann. Phys.* **2008**, *323*, 34–48. [CrossRef]
2. Jiang, H.; Zhang, J.; Lan, D.; Chao, K.K.; Liou, S.; Shahnasser, H.; Fechter, R.; Hirose, S.; Harrison, M.; Roy, S. A low-frequency versatile wireless power transfer technology for biomedical implants. *IEEE Trans. Biomed. Circuits Syst.* **2013**, *7*, 526–535. [CrossRef] [PubMed]

3. Nair, V.V.; Choi, J.R. An Integrated Chip High-Voltage Power Receiver for Wireless Biomedical Implants. *Energies* **2015**, *8*, 5467–5487. [CrossRef]
4. Mizuno, K.; Miyakoshi, J.; Shinohara, N. Wireless power transfer using resonant coupling and in vitro study. In Proceedings of the 2014 IEEE General Assembly and Scientific Symposium, Beijing, China, 16–23 August 2014; pp. 97–107.
5. Cruciani, S.; Campi, T.; Maradei, F.; Feliziani, M. Numerical simulation of Wireless Power Transfer system to recharge the battery of an implanted cardiac pacemaker. In Proceedings of the International Symposium on Electromagnetic Compatibility, Raleigh, NC, USA, 1–4 September 2014; pp. 44–47.
6. Mizuno, K.; Shinohara, N.; Miyakoshi, J. Expression of Heat Shock Proteins in Human Fibroblast Cells under Magnetic Resonant Coupling Wireless Power Transfer. *Energies* **2015**, *8*, 12020–12028. [CrossRef]
7. Tortora, G.; Mulana, F.; Ciuti, G.; Dario, P.; Menciassi, A. Inductive-Based Wireless Power Recharging System for an Innovative Endoscopic Capsule. *Energies* **2015**, *8*, 10315–10334. [CrossRef]
8. Rao, S.; Chiao, J.C. Body Electric: Wireless Power Transfer for Implant Applications. *IEEE Microw. Mag.* **2015**, *16*, 54–64. [CrossRef]
9. Chen, W.; Liu, C.; Lee, C.; Shan, Z. Cost-Effectiveness Comparison of Coupler Designs of Wireless Power Transfer for Electric Vehicle Dynamic Charging. *Energies* **2016**, *9*, 906. [CrossRef]
10. Song, X.; Liu, G.; Chao, Z.; Xia, H.; Zhang, R.U.; Xu, X.Y. Resonance Wireless Charging Technology in Separate Groups for the Power Battery Packs of Electric Buses. *Diangong Jishu Xuebao* **2013**, *28*, 92–98.
11. Hou, C.C.; Chang, K.Y. Inductive Power Transfer Systems for Bus-Stop-Powered Electric Vehicles. *Energies* **2016**, *9*, 512. [CrossRef]
12. Jang, Y.J.; Jeong, S.; Min, S.L. Initial Energy Logistics Cost Analysis for Stationary, Quasi-Dynamic, and Dynamic Wireless Charging Public Transportation Systems. *Energies* **2016**, *9*, 483. [CrossRef]
13. Naberezhnykh, D.; Theodoropoulos, T.; Reed, N.; Ognissanto, F.; Bludszuweit, H. Operational requirements for dynamic wireless power transfer systems for electric vehicles. In Proceedings of the IEEE Electric Vehicle Conference, Florence, Italy, 17–19 December 2014; pp. 1–8.
14. Batra, T.; Schaltz, E.; Ahn, S. Reduction of magnetic emission by increasing secondary side capacitor for ferrite geometry based series-series topology for wireless power transfer to vehicles. In Proceedings of the European Conference on Power Electronics and Applications, Lappeenranta, Finland, 26–28 August 2014; pp. 1–11.
15. Li, S.; Mi, C.C. Wireless Power Transfer for Electric Vehicle Applications. *IEEE J. Emerg. Sel. Top. Power Electron.* **2015**, *3*, 4–17.
16. Shekhar, A.; Prasanth, V.; Bauer, P.; Bolech, M. Economic Viability Study of an On-Road Wireless Charging System with a Generic Driving Range Estimation Method. *Energies* **2016**, *9*, 76. [CrossRef]
17. Wang, Z.; Wei, X.; Dai, H. Design and Control of a 3 kW Wireless Power Transfer System for Electric Vehicles. *Energies* **2015**, *9*, 10. [CrossRef]
18. Gao, Y.; Farley, K.B.; Tse, Z.T.H. A Uniform Voltage Gain Control for Alignment Robustness in Wireless EV Charging. *Energies* **2015**, *8*, 8355–8370. [CrossRef]
19. Budhia, M.; Boys, J.T.; Covic, G.; Huang, C.-Y. Development of a Single-Sided Flux Magnetic Coupler for Electric Vehicle IPT Charging Systems. *IEEE Trans. Ind. Electron.* **2013**, *60*, 318–328. [CrossRef]